Medical Physics
The International Journal of Medical Physics Research and Practice

Predicting adenocarcinoma recurrence using computational texture models of nodule components in lung CT

Adrien Depeursinge, Masahiro Yanagawa, Ann N. Leung, and Daniel L. Rubin

Citation: Medical Physics **42**, 2054 (2015); doi: 10.1118/1.4916088
View online: http://dx.doi.org/10.1118/1.4916088
View Table of Contents: http://scitation.aip.org/content/aapm/journal/medphys/42/4?ver=pdfcov
Published by the American Association of Physicists in Medicine

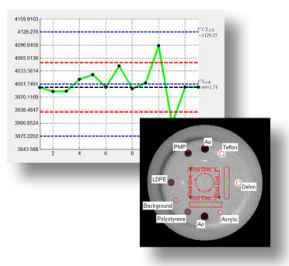

Predicting adenocarcinoma recurrence using computational texture models of nodule components in lung CT

Adrien Depeursinge[a)]
Department of Radiology, Stanford University School of Medicine, Stanford, California 94305 and Business Information Systems, University of Applied Sciences Western Switzerland (HES-SO), Sierre 3960, Switzerland

Masahiro Yanagawa
Department of Radiology, Stanford University School of Medicine, Stanford, California 94305 and Department of Radiology, Osaka University Graduate School of Medicine, Suita, Osaka 565-0871, Japan

Ann N. Leung and Daniel L. Rubin
Department of Radiology, Stanford University School of Medicine, Stanford, California 94305

(Received 7 May 2014; revised 6 February 2015; accepted for publication 15 February 2015; published 30 March 2015)

Purpose: To investigate the importance of presurgical computed tomography (CT) intensity and texture information from ground-glass opacities (GGO) and solid nodule components for the prediction of adenocarcinoma recurrence.
Methods: For this study, 101 patients with surgically resected stage I adenocarcinoma were selected. During the follow-up period, 17 patients had disease recurrence with six associated cancer-related deaths. GGO and solid tumor components were delineated on presurgical CT scans by a radiologist. Computational texture models of GGO and solid regions were built using linear combinations of steerable Riesz wavelets learned with linear support vector machines (SVMs). Unlike other traditional texture attributes, the proposed texture models are designed to encode local image scales and directions that are specific to GGO and solid tissue. The responses of the locally steered models were used as texture attributes and compared to the responses of unaligned Riesz wavelets. The texture attributes were combined with CT intensities to predict tumor recurrence and patient hazard according to disease-free survival (DFS) time. Two families of predictive models were compared: LASSO and SVMs, and their survival counterparts: Cox-LASSO and survival SVMs.
Results: The best-performing predictive model of patient hazard was associated with a concordance index (C-index) of 0.81 ± 0.02 and was based on the combination of the steered models and CT intensities with survival SVMs. The same feature group and the LASSO model yielded the highest area under the receiver operating characteristic curve (AUC) of 0.8 ± 0.01 for predicting tumor recurrence, although no statistically significant difference was found when compared to using intensity features solely. For all models, the performance was found to be significantly higher when image attributes were based on the solid components solely versus using the entire tumors ($p < 3.08 \times 10^{-5}$).
Conclusions: This study constitutes a novel perspective on how to interpret imaging information from CT examinations by suggesting that most of the information related to adenocarcinoma aggressiveness is related to the intensity and morphological properties of solid components of the tumor. The prediction of adenocarcinoma relapse was found to have low specificity but very high sensitivity. Our results could be useful in clinical practice to identify patients for which no recurrence is expected with a very high confidence using a presurgical CT scan only. It also provided an accurate estimation of the risk of recurrence after a given duration t from surgical resection (i.e., C-index $= 0.81 \pm 0.02$).
 [http://dx.doi.org/10.1118/1.4916088]

Key words: lung cancer, texture analysis, steerable Riesz wavelets, quantitative imaging biomarkers, radiomics

1. INTRODUCTION

Adenocarcinoma is a subtype of nonsmall cell lung cancer that begins in the cells that line the alveoli. It is the most common histopathologic subtype of lung cancer, and its incidence is increasing.[1] In 2011, a new classification of the adenocarcinoma subtypes based primarily on histology was proposed to standardize the diagnosis criteria and terminology.[2] Integral to this new classification system is the concept of a spectrum of adenocarcinoma that ranges from preinvasive entities that if resected would have a 100% disease-free survival to frankly invasive adenocarcinoma that has potential to metastasize and result in patient death.

The current approach to evaluate adenocarcinoma aggressiveness is to measure and monitor the size of solid tumor components in thin-section computed tomography (CT) scans.[3,4] However, simple diameter measurement of solid components has shown to have limited reproducibility, where no standardized method is available for part-solid nodules.[5] The monitoring of nodule growth is costly and delivers

significant radiation dose to the patients with repeated CT examinations.[6] The assessment of change in solid tumor size requires a waiting duration of at least one follow-up cycle (e.g., 1–3 months) before treatment when the latter is found to be necessary.

Considerable research efforts have been carried out to enable the assessment of adenocarcinoma aggressiveness based on one single CT study to optimally manage the treatment and follow-up of early lesions. Morphological tissue properties of the tumor are known to be indicators of cancer aggressiveness.[7,8] At the histopathological scale, the various growth patterns of the cancer cells in small peripheral adenocarcinomas have been classified into several categories including lepidic, acinar, papillary, and solid growth.[2] In lepidic predominant adenocarinoma, single-layered cancer cells grow along alveolar walls, and the distance between the alveoli (i.e., septa) is widened. The acinar growth consists of disorganized malignant glands invading a fibrous stroma, which can cause disorientations of fibroblasts and collagen. Papillary patterns are characterized by columnar malignant cells aligning on the surface of fibrovascular structures. Solid growths are cohesive cell agglomerates. Angiogenesis[9,10] and lymphovascular invasion[8] are other histopathological markers of adenocarcinoma aggressiveness causing morphological tissue alterations. Although invisible on CT images, the combinations of these histological patterns (i.e., patchy or mixed) create textured patterns that are characterized in thin-section CT by various proportions and subtypes of ground-glass opacities (GGO) and solid nodule components.[2,8,9] The underlying histopathological patterns also lead to large intraclass variations of GGO and solid components. In GGO, the visible underlying bronchovascular structures from both normal vasculature and increased angiogenesis create even greater variations of its appearance on CT.

The proportions of solid and GGO components are known to be predictors of prognosis.[11,12] Although GGO is an indicator of malignancy,[13] its presence in a malignant nodule is a sign of less aggressive cancer.[5,11,12,14–16] These findings are thus important for the stratification of adenocarcinoma aggressiveness and the risk of relapse based on the CT examination. Various decision algorithms and scores were first proposed based on CT intensities and human interpretation.[5,11,12,14–16] In addition to the distribution of CT intensities, some studies also investigated the value of computerized texture analysis of the nodules (i.e., morphological properties) as an indicator of cancer aggressiveness.[17–21]

The above-mentioned studies demonstrated the feasibility of predicting prognosis based on CT image features, where tumor texture was found to have an important role in characterizing cancer growth patterns. However, the proposed approaches have several limitations hindering the accuracy of predicting clinical outcome. First, in the prior methods, texture properties are most often averaged over the entire tumor (e.g., Refs. 19, 20, 22, and 23) and do not explicitly characterize GGO and solid components. Mattonen *et al.*[21] separated the analysis of tumor components, although focusing on GGO regions only. This limitation has been pointed out recently by Gatenby *et al.*,[24] which recalled that cancer evolution within tumors is directed by complex interactions between many different cell phenotypes with regionally distinct habitats. Second, all texture descriptors used (e.g., fractal dimension and Laplacians of Gaussian or Haralick) are not specifically designed to model GGO and solid components, and may characterize a wide range of morphological properties that are not related to cancer evolution (e.g., CT noise).[25–27]

In this work, we first learn computational texture models of GGO and solid components of lung tumors using steerable second-order Riesz wavelets[28] and linear support vector machines (SVMs). The models obtained have the desirable property of quantifying CT image features that are specific to GGO and solid tissue. Second, responses of the locally steered texture models are combined with HU statistics to predict tumor recurrence and relapse rate (i.e., patient hazard) after a given disease-free survival (DFS) time t. Responses of initial second-order Riesz wavelets are used as a baseline method. The mapping of the descriptors to tumor recurrence and patient hazard is carried out using either a LASSO (Ref. 29) or SVM (Ref. 30) model and their survival counterparts: Cox-LASSO (Ref. 31) or survival SVMs.[32]

2. MATERIALS

In this study, 101 patients with surgically resected stage I adenocarcinoma from Osaka University Hospital were retrospectively reviewed (see Table I). A presurgical CT scan was available for each patient. All patients had undergone lobectomy ($n = 70$) or segmentectomy ($n = 31$). After hospital discharge from resection, patient follow-up was carried out every three months. Additional thoracoabdominal CT scans were generally performed every 6 months. Tumor recurrence was confirmed by CT scan and 18-fluorodeoxyglucose-PET (positron emission tomography) scan when necessary. The median follow-up period of all 101 patients after surgery was 6.03 yr (range of 0.86–12.63 yr). During the follow-up period, 17 patients had disease recurrence with six associated cancer-related deaths. The 84 patients (83.2%) with no observed failure events in the present study were considered censored for disease recurrence. No recurrence was observed in all ten patients with pure GGO nodules, which is in accordance with the previous studies.[11,12] The distribution of the DFS and censoring times is shown in Fig. 1. DFS defines the time interval for which the patient did not have

TABLE I. Patients (101 in total).

Age (years)	63.53 ± 9.81
Women	52 (51.49%)
Median follow-up	6.03 yr
Recurrence during the follow-up period	17 (16.83%)
Censored	84 (83.17%)
Site of recurrence	1 brain, 9 lungs, 3 pleurae, 3 lymph nodes and 1 bone
Pure GGO lesions	10 (9.9%)
Pure solid	44 (43.56%)
Mixed GGO and solid lesions	47 (46.53%)
Maximum total lesion area in slice (mm^2)	158.14 ± 85.31

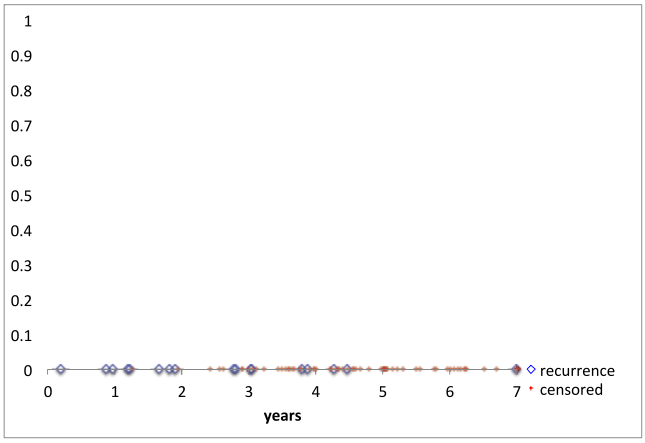

FIG. 1. Distribution of the DFS and censoring times. Time $t = 0$ corresponds to tumor resection.

tumor relapse, whereas censoring denotes the time when the patient left the study. CT scans were reconstructed with slice thicknesses of 0.625–1.25 mm. The pixel spacings are in the range of 0.33–0.43 mm. All CT slices were resampled to have pixel dimensions of 0.33×0.33 mm^2 using bicubic interpolation. This ensures that the physical dimensions (i.e., image scales and directions) are comparable between patients for computerized image analysis on pixel lattices. A thoracic radiologist with 12 yr of experience separately delineated regions of interest (ROIs) for GGO and solid nodule components (see Table II and Fig. 2). The CT slice with maximum total lesion area (solid and GGO components) was chosen for the annotation of the lesion.

3. METHODS

3.A. Computational texture models of nodule components

A texture model that can optimally discriminate between solid and GGO components was built from a linear combination of second-order Riesz wavelets.[33] Riesz wavelets are advantageous for characterizing texture compared the methods used in prior works because they can exhaustively characterize image directions (i.e., steerable property) and scales (i.e., multiresolution). Our hypothesis is that the learned texture models that encompass combinations of image scales and directions that are very specific to GGO and solid tumor components on CT can be useful for predicting clinical outcome. This constitutes an advantage when compared to other texture attributes (e.g., fractal dimension and Laplacians of Gaussian or Haralick), which are arbitrarily characterizing image scales and directions that may be associated to CT noise

TABLE II. ROIs (160 in total).

GGO ROIs	57 (35.62%)
Area of GGO ROI in slice (mm^2)	109.25 ± 64.24
Solid ROIs	103 (64.38%)
Area of solid ROI in slice (mm^2)	97.07 ± 82.61

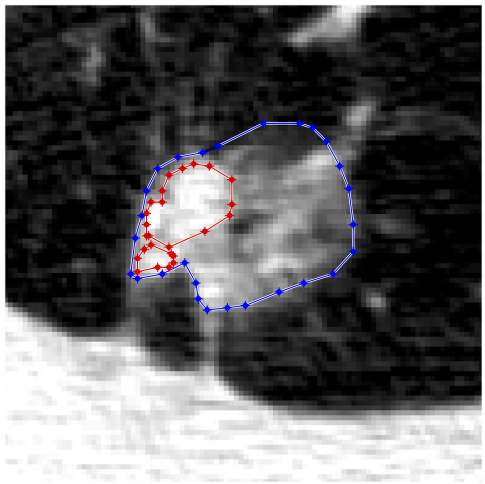

FIG. 2. Example of a lesion with GGO (external boundary) and solid (internal) components annotated. The CT slice where the total lesion area was the largest was selected. The GGO region was excluding the two solid ROIs in this case.

or everything unrelated to the specific properties of GGO and solid tumor tissue. The weights of the linear combination were learned using linear SVMs in a classification configuration opposing GGO versus solid regions. Then, the model obtained and its additive inverse were locally steered to maximize their own magnitudes for each scale (see Secs. 3.A.2 and 3.B). This enabled rotation-covariance,[33] where the characterization of the local texture properties was performed independently from their orientation. The energies of the maximum magnitudes of the models were used as input features for predicting the risk of tumor recurrence using either Cox-LASSO (Ref. 31) or survival SVMs (Ref. 32) (see Sec. 3.C).

3.A.1. Second-order Riesz wavelets

The wavelet functions were derived from the Riesz singular kernels.[28] For a 2-D signal $f(x)$, the kernels of the second-order Riesz transform $\mathcal{R}^2$ are defined as

$$\mathcal{R}^2\{f\}(x) = \begin{pmatrix} \mathcal{R}^{(0,2)}\{f\}(x) \\ \mathcal{R}^{(1,1)}\{f\}(x) \\ \mathcal{R}^{(2,0)}\{f\}(x) \end{pmatrix}. \quad (1)$$

The three singular kernels $\mathcal{R}^{(n,2-n)}\{f\}(x)$, $n = 0, 1, 2$ are defined in the Fourier domain as

$$\mathcal{R}^{(n,2-n)}\{f\}(x) \overset{\mathcal{F}}{\longleftrightarrow} \widehat{\mathcal{R}^{(n,2-n)}\{f\}}(\omega), \quad (2)$$

where

$$\widehat{\mathcal{R}^{(n,2-n)}\{f\}}(\omega) = \sqrt{\frac{2}{n!(2-n)!}} \frac{(-j\omega_1)^n(-j\omega_2)^{2-n}}{\|\omega\|^2} \hat{f}(\omega), \quad (3)$$

with $\omega_{1,2}$ corresponding to the frequencies along the two image axes $x_{1,2}$. The multiplication with $j\omega_{1,2}$ in the numerator corresponds to partial derivatives of f, and the division by the norm of ω in the denominator makes that only phase information (i.e., image directions) is retained. Wavelet filters can be obtained by convolving the Riesz kernels with isotropic

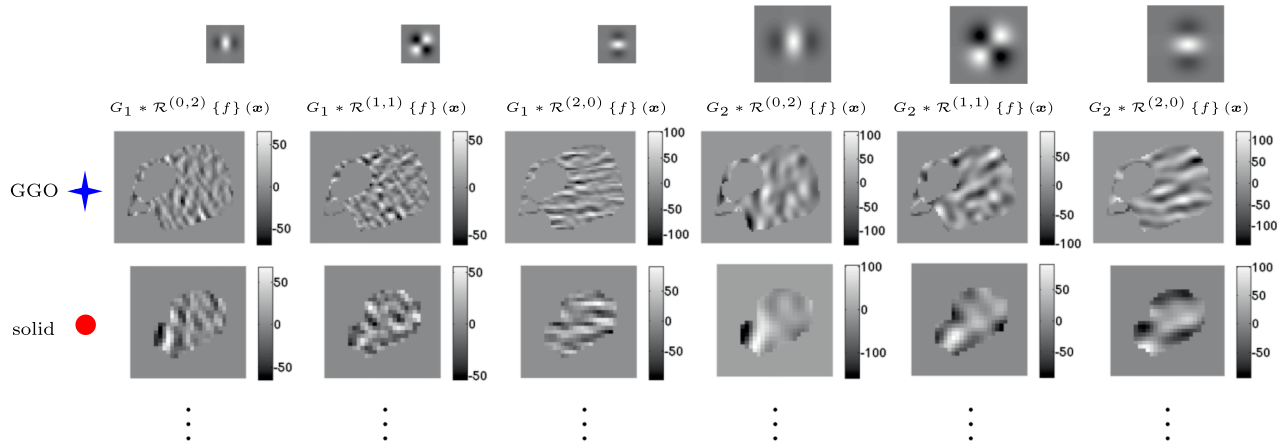

FIG. 3. Expression of GGO and solid regions in terms of their corresponding multiscale and multidirectional Riesz coefficients. The Riesz kernels can decompose image scales and directions into distinct sub-bands.

band-limited wavelets G_k with $k = 1,\ldots,K$ being the number of decomposition levels (i.e., image scales).[28] Simoncelli's dyadic multiresolution framework with an undecimated transform (i.e., frames) was used in this work.[34]

3.A.2. Steerable texture models

A texture model Γ was built from a linear combination of multiscale Riesz wavelets as

$$\begin{aligned}\Gamma &= \mathbf{w}^T G_k * \mathcal{R}^2 \\ &= w_1 G_1 * \mathcal{R}^{(0,2)} + \cdots + w_6 G_K * \mathcal{R}^{(2,0)}.\end{aligned} \tag{4}$$

The vector $\mathbf{w}$ was learned using linear SVMs as the direction vector of a maximal margin separating hyperplane between GGO (i.e., treated as the negative class) versus solid (i.e., positive class) regions. The regions were expressed in a feature space spanned by the energies E of respective the wavelet sub-bands as $E\big(G_k * \mathcal{R}^{(n,2-n)}\{f\}(x)\big)$. The wavelet coefficients are shown in Fig. 3, and the model learning process is illustrated in Fig. 4.

The steerable property of Riesz wavelets was leveraged to enable the synthesis of any orientation of the model Γ_k^θ from a linear combination of the Riesz wavelets as

$$\Gamma_k^\theta = \mathbf{w}_k^{\mathrm{T}} G_k * A^\theta \mathcal{R}^2, \tag{5}$$

where $\mathbf{w}_k$ contains the weights of the wavelet sub-bands from the decomposition level k. A^θ is a steering matrix depending only on θ as

$$A^\theta = \begin{pmatrix} \cos^2\theta & \sqrt{2}\cos\theta\sin\theta & \sin^2\theta \\ -\sqrt{2}\cos\theta\sin\theta & \cos^2\theta - \sin^2\theta & \sqrt{2}\cos\theta\sin\theta \\ \sin^2\theta & -\sqrt{2}\cos\theta\sin\theta & \cos^2\theta \end{pmatrix}. \tag{6}$$

3.B. Texture features

Two groups of texture features based on Riesz wavelets were compared. First, the energies of the Riesz wavelets as $E\big(G_k * \mathcal{R}^2\{f\}(x)\big)$ were used as a baseline. This feature group is referred to as *initial Riesz* and had a dimensionality of $3K$. Second, rotation-covariant features from locally steered models were used and are referred to as *steered models*. The scalewise models Γ_k were locally steered to maximize their magnitude for each decomposition level. This allows, at a fixed scale, to locally align all wavelet coefficients consistently based on the directional profiles of the learned models. It therefore can analyze the local hierarchical organization of image directions independently from their local orientation, which proved to outperform approaches that are characterizing the global distributions of image directions (e.g., initial Riesz, Haralick, and histogram of gradients). This property is called "rotation-covariance."[33]

The maximum magnitude $m_{\max}$ of the model Γ_k at the position x_p is

$$m_{\max}(\Gamma_k, x_p) = \arg\max_{\theta\in[0,\pi]} \big(\mathbf{w}_k^{\mathrm{T}} G_k * (A^\theta \mathcal{R}^2)\{f\}\big)(x_p). \tag{7}$$

Features from the steered models were defined as the energies of scalewise magnitude maps: $E(m_{\max}(\Gamma_k, x))$. This resulted in a dimensionality of $2K$ while considering the models $\Gamma_{k=1,\ldots,K}$ and their additive inverses (i.e., $\Gamma_1^{\mathrm{GGO}} = -\Gamma_1^{\mathrm{solid}}$).

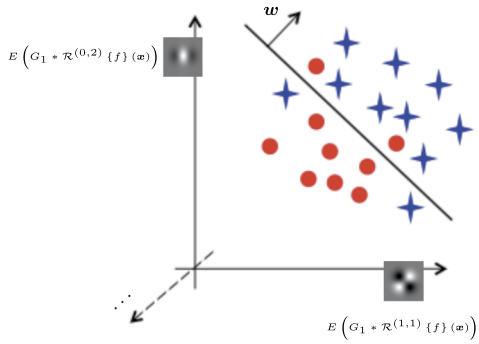

FIG. 4. Learning of the multiscale model Γ from a linear combination of the initial Riesz wavelets. Γ is characterized by the direction vector $\mathbf{w}$ [see Eq. (4)], which was learned using linear SVMs in a classification configuration opposing GGO (dots) versus solid (stars) regions. This step allows identifying the linear combinations of image scales and directions that are specific to GGO and solid tumor tissue in CT.

3.C. Predictive models

Two types of predictive models were compared for the classification of patient i into the class $y_i = 1$ (i.e., tumor recurrence) versus $y_i = -1$ (i.e., no recurrence): LASSO (Ref. 29) and kernel SVMs.[30] We also compared two different predictive models for mapping of the feature vectors $\mathbf{v}$ defined in Sec. 3.B to relapse rate for a given DFS time t: Cox-LASSO (Ref. 31) and kernel survival SVMs.[32] The survival analysis paradigm was considered with data in the form $(t,\mathbf{v},\boldsymbol{\delta})$, where $\boldsymbol{\delta}$ is a binary vector, where 1 corresponds to a failure and 0 to censoring.[31] In this case, the survival models predict the patient hazard $h_i(t)$, which measures the failure rate for a fixed DFS time t. A patient a associated with a hazard value $h_a(t) > h_b(t)$ is expected to have a tumor recurrence earlier than patient b. $h_i(t)$ provides a better estimate of the risk of tumor recurrence when compared to the prediction of the binary class y_i because it can be refined with the time elapsed from surgery.

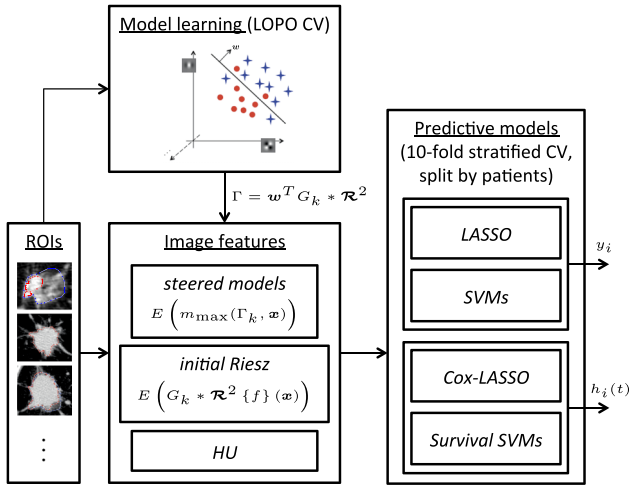

FIG. 5. Flow chart of the experimental setup, starting from the input ROIs to the predicted patient class y_i or hazard $h_i(t)$.

3.C.1. Cox-LASSO

The Cox proportional hazards model assumes that the hazard $h_i(t)$ of the patient i at the time t is

$$h_i(t) = h_0(t)e^{\boldsymbol{\beta}^T\mathbf{v}_i}, \tag{8}$$

where $h_0(t)$ is a hazard baseline shared by all patients. $\boldsymbol{\beta}$ contains the respective weights of each feature and is estimated by maximizing the partial likelihoods of outcomes δ_i for each patient in the training set.[31] A l_1 penalty of the Cox model is used to restrict the sum of $|\boldsymbol{\beta}|$, hence the Cox-LASSO denomination.

3.C.2. Survival SVMs

Survival SVMs extend the concept of margin maximization to survival data. At every event time t, a hyperplane is constructed to separate patients with failure from patients with censoring.[32] The model consists of several hyperplanes (one for each event time) that are parallel and therefore using an identical direction vector $\boldsymbol{\beta}$. This is an analogy to the Cox model where the same $\boldsymbol{\beta}$ is used for all events as well. Using the kernel trick, the kernelized hazard function is defined as

$$h_i(t) = K(\boldsymbol{\beta},\mathbf{v}_i) - b(t), \tag{9}$$

where $b(t)$ defines the offsets of the hyperplanes. The Gaussian kernel $K(\mathbf{v}_i,\mathbf{v}_j) = \exp(-\|\mathbf{v}_i - \mathbf{v}_j\|^2/2\sigma_K^2)$ was used in this work.

3.D. Experimental setup

The flow chart of the experimental setup is depicted in Fig. 5. A total of no more than two decomposition levels (i.e., $K = 2$) were used to limit the influence of objects surrounding the tumor on the local texture properties of the nodule components (e.g., lung boundary and airways). The multiscale texture model Γ_i was learned using linear SVMs for each fold of a leave-one-patient-out (LOPO) cross-validation (CV). For each patient i, the *steered models* features were therefore obtained using all other patients to learn $\mathbf{w}$. Twenty histogram bins of the intensity distribution in $[-1000, 400]$ HU were used as additional features, which we found to be complementary to the Riesz models in Depeursinge *et al.*[27] This feature group is referred to as *HU*. In order to build and evaluate the predictive models, a ten-fold stratified CV was used to balance class cardinalities and the number of patients with failures and censoring in the training and test sets. The data were also separated by patients to ensure that all instances from the same patient are contained either in the training or the test set. Twenty repetitions of the CV were used as it was found to provide a reproducible estimation of the performance based on preliminary tests. The area under a receiver operating characteristic (ROC) curve (AUC) was used to quantify the performance of the binary classification using LASSO and SVMs. The concordance index (C-index) was used to measure the performance of the survival models.[35] It computes the proportion of all patient pairs with at least one of whom had recurrence and in which $h_i(t)$ and DFS times are concordant. Concordance was achieved when the predicted hazard $h_i(t)$ was found to be smaller for the patient with a larger DFS time. The C-index of a model yielding random predictions is 0.5, and it can be interpreted as an AUC for continuous (i.e., noncategorical) outcomes. The *glmnet* R package was used for the implementation of Cox-LASSO.[29,31] Since the number of features was smaller than the number of patients, the regularization parameter λ (i.e., the coefficient of the l_1 penalty in LASSO) was chosen to keep all features in the predictive model. Preliminary testing revealed that the C-index from the test set was maximum with smallest values of λ, which suggested that the model was not overfitting the data. The *survpack* R package was used for the implementation survival SVMs.[32] *LibSVM* was used for the implementation of two-class SVMs.[30] For both two-class and survival SVMs, the cost C of the errors and the variance σ_K of the Gaussian kernel were optimized as $C \in [10^0; 10^3]$ and $\sigma_K \in [10^{-3}; 10^4]$, respectively. For each fold

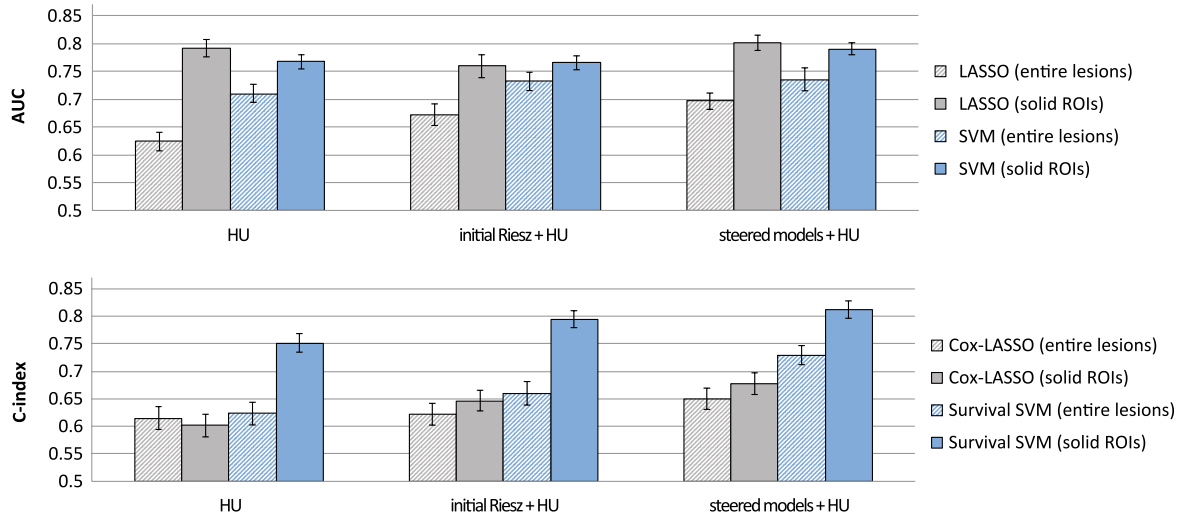

FIG. 6. Performance of the predictive models using various combination of the feature groups. Using solid components solely, the feature space concatenating *steered models* and *HU* yielded the best estimation of tumor recurrence and patient hazard, allowing an average AUC of 0.8 ± 0.01 (LASSO) and an average C-index of 0.81 ± 0.02 (survival SVMs).

of the ten-fold CV, the model built with the value couple (C,σ_K) that provided best training performance was used to predict outcomes of the test instances. Statistical analyses of the comparisons among the predictive performances from (1) feature groups (i.e., *HU* vs *initial Riesz + HU* vs *steered models + HU*), (2) tumor components (i.e., entire lesions vs solid ROIs), and (3) predictive models (i.e., SVMs vs LASSO and survival SVMs vs Cox-LASSO) were carried out using paired t-tests based on the distributions of the estimated AUCs and C-indices (i.e., 200 observations for each model).

4. RESULTS

We compared the performance of the proposed approach when using either the ROI delineating the entire region, or using solid components solely. A subset of 91 patients was used with the exclusion of the 10 patients with pure GGO (i.e., no solid components). The performance of the predictive models using various combinations of the feature groups is shown in Fig. 6. The AUC and C-indices were averaged over the 20 repetitions of the ten folds of the CV (i.e., 200 observations). The error bars are showing the standard errors. Predictive performance using entire lesions (hatched bars) was compared to using solid components solely (plain bars).

The best separation between patients with and without recurrence (i.e., AUC $= 0.8 \pm 0.014$) was obtained with the *steered models* and *HU* from solid components and LASSO. However, no statistical difference was found when compared to using *HU* solely for this task ($p = 0.12$). The use of solid components solely outperformed entire lesions for all image-based feature groups when using LASSO ($p < 5.73 \times 10^{-28}$) or SVMs ($p < 5.35 \times 10^{-6}$). The best prediction of the patient hazard (i.e., C-index of 0.81 ± 0.02) was obtained with *steered models* and *HU* from solid components and survival SVMs. The latter outperformed the Cox-LASSO models for all feature groups ($p < 1.65 \times 10^{-7}$ when using solid ROIs). Similarly to the binary classification case, the use of solid components solely outperformed entire lesions for all image-based feature groups when using survival SVMs ($p < 3.08 \times 10^{-5}$). The performance gain when using texture information was found to be statistically significant when using *steered models* ($p = 0.0056$ for *HU* versus *steered models + HU* using survival SVMs), but not when using *initial Riesz* ($p = 0.0646$ for *HU* versus *initial Riesz + HU* using survival SVMs).

The decision values and associated ROC of SVMs based on *steered models* and *HU* are shown in Fig. 7. This "score" can predict patients with recurrence with low specificity but very high sensitivity. In other words, patients with low values of this score may be confidently predicted to have disease that will not recur.

To investigate the importance of texture model learning, we compared them with the performance obtained with randomly generated values for $\mathbf{w}$. The associated results are shown in Fig. 8.

The influence of the slice selection for the annotation of GGO and solid components was investigated. For one patient, the regions were identified in each slice containing tumor tissue. A total of 34 GGO regions and 16 solid regions were delineated in 34 consecutive slices. The normalized distributions of the feature values from GGO versus solid regions across tumor slices are shown in Fig. 9. The interslice variability of the feature values is found to be small when compared to the feature differences between GGO and solid tissue. The vertical lines in Fig. 9 show the feature values from the slice with maximum tumor area, which suggests that the latter has feature values within the range of those from the entire tumor, and close to the mean for most parameters. The CT intensity (i.e., *HU*) is higher for solid regions. The energy of the steered model [i.e., $E(m_{\max}(\Gamma_k, x))$] is found to be smaller for solid regions for the two scales $k = 1, 2$, which demonstrates that the solid regions have a more homogeneous texture than GGO.

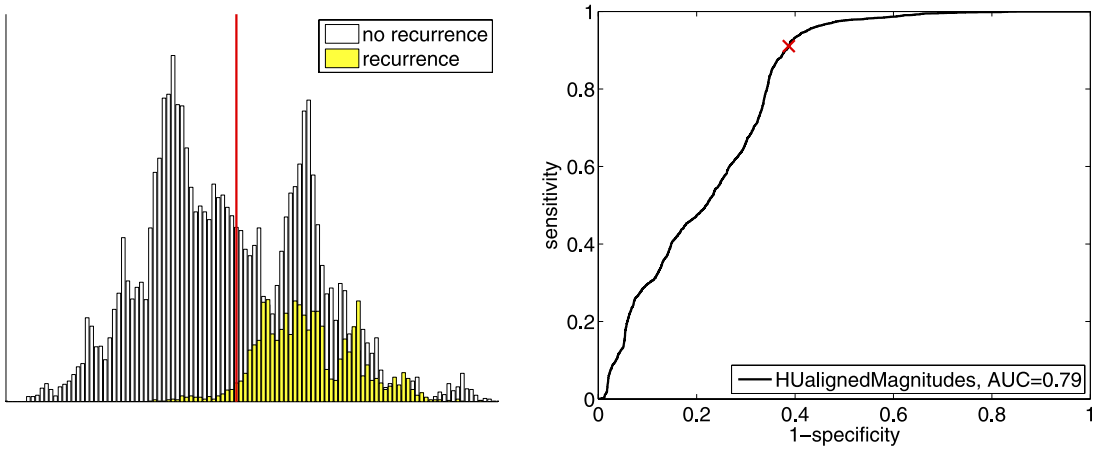

FIG. 7. Distribution of the decision values and associated ROC curve using *steered models* and *HU* from solid components and SVMs. The prediction of patient with recurrence is found to have a low specificity but a very high sensitivity. The specificity and sensitivity for a fixed threshold x_0 of the decision value are 0.61 and 0.91, respectively. This result could be useful for developing a test that can be used in clinical practice to identify patients for which no recurrence is expected with very high confidence using a presurgical CT scan only.

The influence of the precision of the contours drawn by the user to delineate GGO and solid components was investigated. Random drifts in $[-d, d]$ were added to both coordinates of the vertices of the polygons defining ROIs to simulate inaccurate contours. The associated performance for $d = \pm 0,\ldots,6$ mm is detailed in Fig. 10. The choice for the range of deviations was based on Mattonen *et al.*[21] and Xu *et al.*,[36] which stated that interobserver variations in delineation are in the order of $0.1 \cdot R_{\max}$, where $R_{\max}$ is the maximum diameter of the lesion.

5. DISCUSSION AND CONCLUSIONS

We used texture-based computational models of GGO and solid tumor components as well as HU intensity distributions in CT to predict postsurgical tumor recurrence and patient hazards based on DFS times. The cornerstone of our approach is to separate the analysis of nodule subregions to prevent the averaging of image properties over the entire lesions. The best-performing predictive models were based on a combination of CT intensities and the responses of steered texture models of GGO and solid components. It allowed a predictive performance of tumor recurrence associated with an AUC of 0.8 ± 0.01. The prediction of the relapse rate based on DFS times (i.e., patient hazard) is associated with a *C*-index of 0.81 ± 0.02. Figure 7 shows that the proposed approach could identify patients with recurrence with very high sensitivity. This result could be useful for developing a test that can be used in clinical practice to identify patients for which no recurrence is expected with very high confidence from presurgical CT only. Moreover, the prediction of the patient hazard using the survival models might be used after surgery to continuously assess the risk of cancer relapse for a given time t elapsed from the date of surgery. The latter could be an important clinical tool for the management of patient follow-up and postsurgical treatment options.

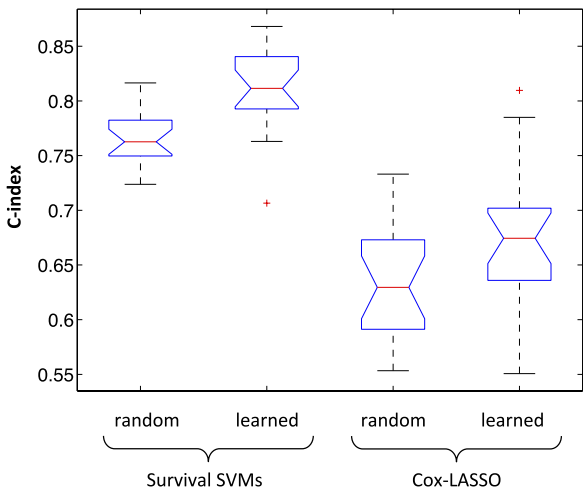

FIG. 8. Performance obtained with random models versus learned models using *steered models* + *HU* from solid ROIs (20 repetitions of the CV). The null hypothesis that the random models can perform as well as the learned ones are rejected for survival SVMs ($p = 5.72 \times 10^{-4}$) and Cox-LASSO ($p = 0.0174$).

When compared to using intensities alone (i.e., *HU*), the performance gain when adding texture attributes (i.e., *steered models* + *HU*) to the predictive model was not found to be statistically significant for the prediction of tumor recurrence with LASSO ($p = 0.12$). However, the performance gain was significant for predicting tumor recurrence with SVMs ($p = 8.64 \times 10^{-6}$). It was also significant for predicting patient hazard using Cox-LASSO ($p = 0.0074$) or survival SVMs ($p = 0.0056$). Texture attributes from *initial Riesz* did not improve the performance when compared to *HU* both for the prediction of tumor recurrence and patient hazard. This suggests that texture information plays an important role but should specifically model morphological tissue properties that are related to adenocarcinoma cancer growth patterns (i.e., GGO and solid textures). This was also confirmed by the performance analysis of randomly generated models in Fig. 8, which isolated the contribution of rotation-covariance [i.e., local steering of the texture models in Eq. (7)] and

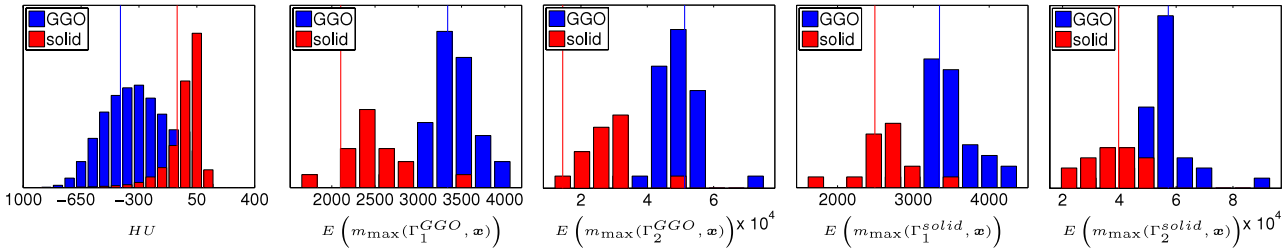

FIG. 9. Normalized distributions of the feature values from GGO versus solid regions across tumor slices of one patient. The vertical lines show the feature value for the slice with maximum total tumor area, which was selected for the analysis. The interslice variability of the features is found to be small, where the distribution of features from GGO (blue) and solid (red) remain distinct across every axial slice of the tumor.

texture model learning. The null hypothesis that the random models can perform as well as the learned ones are rejected for both survival SVMs ($p = 5.72 \times 10^{-4}$) and Cox-LASSO ($p = 0.0174$). These results highlight the importance of using texture attributes that are specifically designed to model CT image features of tissue of interest (i.e., GGO and solid), when compared to other studies based on general purpose attributes (e.g., fractal dimension and Laplacians of Gaussian or Haralick).[25–27]

The predictive models based on solid components solely outperformed others based on entire ROIs with statistical significance for all image-based feature groups ($p < 3.08 \times 10^{-5}$). This demonstrates the importance of separating the computerized analyses of CT regions from GGO and solid components to assess adenocarcinoma cancer aggressiveness.[24] A majority of studies focused on the ratio of GGO and solid quantities,[5,11,12,14–16] whereas our work provides a novel perspective on how to interpret imaging information from CT examinations by suggesting that most of the information related to adenocarcinoma aggressiveness is located in the solid components of the tumor.

The analysis of the feature values across tumor CT slices from one patient suggests that the slice with maximum total axial tumor area provided feature values that are close to the mean for most attributes (see Fig. 9). However, the selected slice may not be representative of the total feature variation throughout the entire tumor, which we plan to investigate using 3-D texture attributes in future work. We found our proposed predictive model to be robust to a contour precision of 4 mm for the delineation of the GGO and solid nodule components (see Fig. 10). This is consistent with the findings of Mattonen *et al.*[21] and suggests that our methods can provide reproducible results even when there is a moderate variation in delineation of the lesion boundary. Xu *et al.*[36] suggested that with maximum diameters R_{max} in the range of 30–70 mm for GGO regions and 10–40 mm for solid components; interobserver variations of 3–7 mm for GGO and 1–4 mm for solid are expected (i.e., $0.1 \cdot R_{max}$). A contour precision of 4 mm is therefore acceptable for solid but not for GGO. However, since our model showed to provide best performance using solid regions only, the clinicians will need only to delineate solid regions, whereas a separated high-quality subset can be used to learn the texture models for GGO and solid.

Our results are aligned with best performance reported in the literature (see Table III), but yet it is challenging to

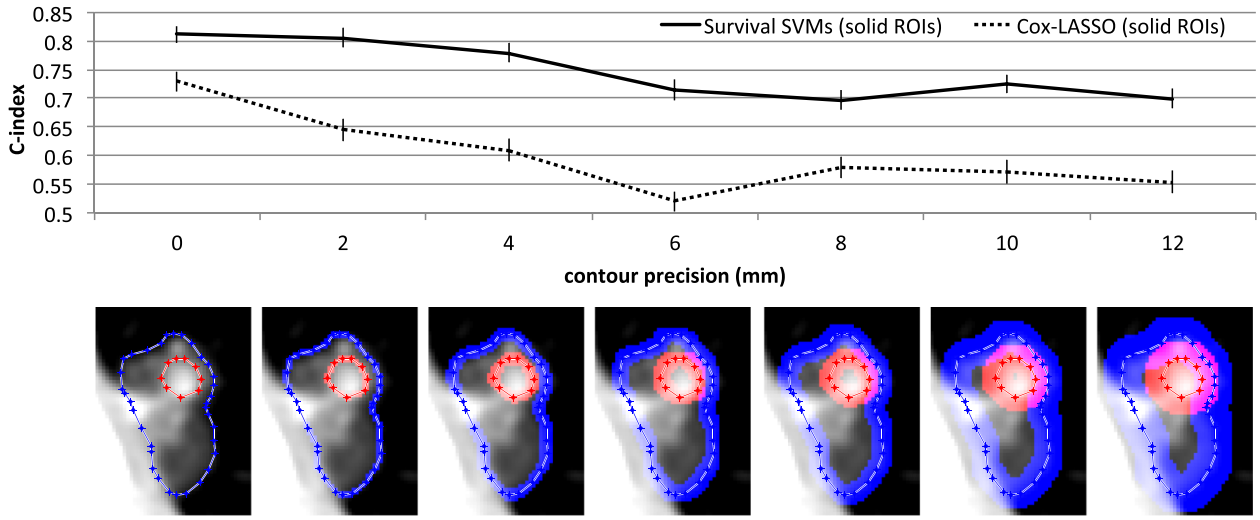

FIG. 10. Influence of the precision of the contours drawn by the user to delineate GGO and solid components using *steered models + HU*. Random drifts of the vertices of the polygons defining ROIs were used to simulate inaccurate contours. Only solid ROIs are used for the predictive models in this case, but we recall that both GGO and solid ROIs are used to learn the texture models (see Fig. 5). The approach showed to be robust to deviations smaller than 4 mm for survival SVMs.

TABLE III. Performance comparison with other studies predicting tumor aggressiveness, recurrence, and patient survival.

Study	Number of patients	Predicted outcome	Separation of tumor components	Reported performance
Al-Kadi and Watson (Ref. 22)	15	Aggressive vs less aggressive adenocarinoma	No	0.83 (accuracy)
Ganeshan *et al.* (Ref. 19)	17	Below vs above stage II	No	0.7 (kappa)
Ganeshan *et al.* (Ref. 20)	54	Low vs high survival	No	0.6 (AUC)
Matsuguma *et al.* (Ref. 16)	383	Aggressive vs less aggressive adenocarinoma	Yes	0.85 (AUC)
Mattonen *et al.* (Ref. 21)	46	Tumor recurrence (yes/no)	Yes	0.8 (AUC)
This work	91	Tumor recurrence (yes/no)	Yes	0.79 (AUC)
This work	91	Tumor recurrence (patient hazard)	Yes	0.81 (*C*-index)

compare the performance between studies that were based on different case data and/or definition of the outcome variable. The approaches proposed by Al-Kadi and Watson[22] and Ganeshan *et al.*[19] are based on texture properties measured over entire 2-D ROIs delineated in the slice with largest transverse dimension of the tumor. The influence of the choice of the slice on prediction performance may be larger when compared to our study since they do not separate GGO and solid regions. Mixing the two types of tissue may lead to very large variations of the image attributes from one slice to another since a larger proportion of solid regions will result in an increased CT intensity and a decreased texture heterogeneity (see Fig. 9). Neither of the two studies evaluated the variation of the image attributes over the different slices of the tumors. They both also evaluated their methods on a small number of patients (i.e., 15 in Al-Kadi and Watson[22] and 17 in Ganeshan *et al.*[19]). Matsuguma *et al.*[16] used the proportion of GGO and solid areas to differentiate between aggressive and less aggressive adenocarcinoma. A major limitation of their study is that they estimated the proportion of tumor components from a single axial slice, which may strongly vary from on slice to another. Mattonen *et al.*[21] used 2-D texture features extracted from every slices of the tumors to predict tumor recurrence with a high success rate (AUC = 0.8). However, their approach is based on post-treatment scans (i.e., 2–5 and 5–8 months after the beginning of stereotactic ablative radiotherapy), which can be considered as an easier task when compared to using presurgical scans only.

We recognize several limitations of the current work, including the choice of the CT slice for tumor delineation with maximum total tumor area and the use of 2-D texture descriptors, which can both potentially entail a large reduction of the information exploited. The patients were not stratified by lobectomy versus segmentectomy, which could also have a potential impact on the result obtained. Future work will include validating our results in an independent data set with automated volumetric segmentation of homogeneous nodule components (e.g., using supervoxels[37] or voxel-based classification[38]) with an increased granularity when compared to using GGO and solid regions. Multiple readers will be recruited to evaluate the interobserver variation in drawing GGO and solid parts of the tumor. 3-D texture analysis will be used to fully leverage the volumetric data. We also plan to investigate the ability of this approach to differentiate between dominant underlying histopathological categories of cell growth patterns (e.g., lepidic, acinar, papillary, and solid) from CT data alone.

ACKNOWLEDGMENTS

This work was supported by the Swiss National Science Foundation (under Grant Nos. PBGEP2_142283, PZ00P2_154891, and 205320_141300/1), and the National Cancer Institute, National Institutes of Health (U01-CA-142555).

[a)]Author to whom correspondence should be addressed. Electronic mail: adrien.depeursinge@hevs.ch

[1]S. H. Barsky, R. Cameron, K. E. Osann, D. Tomita, and E. Carmack Holmes, "Rising incidence of bronchioloalveolar lung carcinoma and its unique clinicopathologic features," Cancer **73**, 1163–1170 (1994).

[2]W. D. Travis, E. Brambilla, M. Noguchi, A. G. Nicholson, K. R. Geisinger, Y. Yatabe, D. G. Beer, C. A. Powell, G. J. Riely, P. E. Van Schil, K. Garg, J. H. M. Austin, H. Asamura, V. W. Rusch, F. R. Hirsch, G. Scagliotti, T. Mitsudomi, R. M. Huber, Y. Ishikawa, J. Jett, M. Sanchez-Cespedes, J.-P. Sculier, T. Takahashi, M. Tsuboi, J. Vansteenkiste, I. Wistuba, P.-C. Yang, D. Aberle, C. Brambilla, D. Flieder, W. Franklin, A. Gazdar, M. Gould, P. Hasleton, D. Henderson, B. Johnson, D. Johnson, K. Kerr, K. Kuriyama, J. S. Lee, V. A. Miller, I. Petersen, V. Roggli, R. Rosell, N. Saijo, E. Thunnissen, M. Tsao, and D. Yankelewitz, "International association for the study of lung cancer/American thoracic society/European respiratory society international multidisciplinary classification of lung adenocarcinoma," J. Thorac. Oncol. **6**, 244–285 (2011).

[3]D. P. Naidich, A. A. Bankier, H. MacMahon, C. M. Schaefer-Prokop, M. Pistolesi, J. M. Goo, P. Macchiarini, J. D. Crapo, C. J. Herold, J. H. Austin, and W. D. Travis, "Recommendations for the management of subsolid pulmonary nodules detected at CT: A statement from the Fleischner society," Radiology **266**, 304–317 (2013).

[4]K. H. Lee, J. M. Goo, S. J. Park, J. Y. Wi, D. H. Chung, H. Go, H. S. Park, C. M. Park, and S. M. Lee, "Correlation between the size of the solid component on thin–section CT and the invasive component on pathology in small lung adenocarcinomas manifesting as ground–glass nodules," J. Thorac. Oncol. **9**, 74–82 (2014).

[5]M. Yanagawa, Y. Tanaka, A. N. Leung, E. Morii, M. Kusumoto, S. Watanabe, H. Watanabe, M. Inoue, M. Okumura, T. Gyobu, K. Ueda, O. Honda, H. Sumikawa, T. Johkoh, and N. Tomiyama, "Prognostic importance of volumetric measurements in stage I lung adenocarcinoma," Radiology **272**, 557–567 (2014).

[6]H. MacMahon, J. H. M. Austin, G. Gamsu, C. J. Herold, J. R. Jett, D. P. Naidich, E. F. Patz, S. J. Swensen, and null, "Guidelines for management of small pulmonary nodules detected on CT scans: A statement from the Fleischner society," Radiology **237**, 395–400 (2005).

[7]T. Yokose, K. Suzuki, K. Nagai, Y. Nishiwaki, S. Sasaki, and A. Ochiai, "Favorable and unfavorable morphological prognostic factors in peripheral

adenocarcinoma of the lung 3 cm or less in diameter," Lung Cancer **29**, 179–188 (2000).
[8]K. Suzuki, M. Kusumoto, S. Watanabe, R. Tsuchiya, and H. Asamura, "Radiologic classification of small adenocarcinoma of the lung: Radiologic–pathologic correlation and its prognostic impact," Ann. Thorac. Surg. **81**, 413–419 (2006).
[9]U. Tateishi, H. Nishihara, S. Watanabe, T. Morikawa, K. Abe, and K. Miyasaka, "Tumor angiogenesis and dynamic CT in lung adenocarcinoma: Radiologic—pathologic correlation," J. Comput. Assisted Tomogr. **25**, 23–27 (2001).
[10]A.-P. Meert, M. Paesmans, B. Martin, P. Delmotte, T. Berghmans, J.-M. Verdebout, J.-J. Lafitte, C. Mascaux, and J.-P. Sculier, "The role of microvessel density on the survival of patients with lung cancer: A systematic review of the literature with meta–analysis," Br. J. Cancer **87**, 694–701 (2002).
[11]K. Kodama, M. Higashiyama, H. Yokouchi, K. Takami, K. Kuriyama, M. Mano, and T. Nakayama, "Prognostic value of ground–glass opacity found in small lung adenocarcinoma on high-resolution CT scanning," Lung Cancer **33**, 17–25 (2001).
[12]K. Suzuki, H. Asamura, M. Kusumoto, H. Kondo, and R. Tsuchiya, "Early peripheral lung cancer: Prognostic significance of ground glass opacity on thin–section computed tomographic scan," Ann. Thorac. Surg. **74**, 1635–1639 (2002).
[13]C. I. Henschke, D. F. Yankelevitz, R. Mirtcheva, G. McGuinness, D. McCauley, and O. S. Miettinen, "CT screening for lung cancer: Frequency and significance of part–solid and nonsolid nodules," Am. J. Roentgenol. **178**, 1053–1057 (2014).
[14]H. Matsuguma, R. Nakahara, M. Anraku, T. Kondo, Y. Tsuura, Y. Kamiyama, K. Mori, and K. Yokoi, "Objective definition and measurement method of ground–glass opacity for planning limited resection in patients with clinical stage IA adenocarcinoma of the lung," Eur. J. Cardio-Thorac. Surg. **25**, 1102–1106 (2004).
[15]M. Yanagawa, Y. Tanaka, M. Kusumoto, S. Watanabe, R. Tsuchiya, O. Honda, H. Sumikawa, A. Inoue, M. Inoue, M. Okumura, N. Tomiyama, and T. Johkoh, "Automated assessment of malignant degree of small peripheral adenocarcinomas using volumetric CT data: Correlation with pathologic prognostic factors," Lung Cancer **70**, 286–294 (2010).
[16]H. Matsuguma, I. Oki, R. Nakahara, H. Suzuki, T. Kasai, Y. Kamiyama, S. Igarashi, K. Mori, S. Endo, and K. Yokoi, "Comparison of three measurements on computed tomography for the prediction of less invasiveness in patients with clinical stage I non—small cell lung cancer," Ann. Thorac. Surg. **95**, 1878–1884 (2013).
[17]S. Kido, K. Kuriyama, M. Higashiyama, T. Kasugai, and C. Kuroda, "Fractal analysis of small peripheral pulmonary nodules in thin–section CT: Evaluation of the lung–nodule interfaces," J. Comput. Assisted Tomogr. **26**, 537–578 (2002).
[18]S. Kido, K. Kuriyama, M. Higashiyama, T. Kasugai, and C. Kuroda, "Fractal analysis of internal and peripheral textures of small peripheral bronchogenic carcinomas in thin–section computed tomography: Comparison of bronchioloalveolar cell carcinomas with nonbronchioloalveolar cell carcinomas," J. Comput. Assisted Tomogr. **27**, 56–61 (2003).
[19]B. Ganeshan, S. Abaleke, R. C. D. Young, C. R. Chatwin, and K. A. Miles, "Texture analysis of non–small cell lung cancer on unenhanced computed tomography: Initial evidence for a relationship with tumour glucose metabolism and stage," Cancer Imaging **10**, 137–143 (2010).
[20]B. Ganeshan, E. Panayiotou, K. Burnand, S. Dizdarevic, and K. A. Miles, "Tumour heterogeneity in non–small cell lung carcinoma assessed by CT texture analysis: A potential marker of survival," Eur. Radiol. **22**, 796–802 (2012).
[21]S. A. Mattonen, D. A. Palma, C. J. A. Haasbeek, S. Senan, and A. D. Ward, "Early prediction of tumor recurrence based on CT texture changes after stereotactic ablative radiotherapy (SABR) for lung cancer," Med. Phys. **41**, 033502 (14pp.) (2014).
[22]O. S. Al-Kadi and D. Watson, "Texture analysis of aggressive and nonaggressive lung tumor CE CT images," IEEE Trans. Biomed. Eng. **55**, 1822–1830 (2008).
[23]B. Ganeshan, V. Goh, H. C. Mandeville, Q. S. Ng, P. J. Hoskin, and K. A. Miles, "Non—small cell lung cancer: Histopathologic correlates for texture parameters at CT," Radiology **266**, 326–336 (2013).
[24]R. A. Gatenby, O. Grove, and R. J. Gillies, "Quantitative imaging in cancer evolution and ecology," Radiology **269**, 8–14 (2013).
[25]S. G. Mougiakakou, I. K. Valavanis, A. Nikita, and K. S. Nikita, "Differential diagnosis of CT focal liver lesions using texture features, feature selection and ensemble driven classifiers," Artificial Intell. Med. **41**, 25–37 (2007).
[26]U. Bagci, J. Yao, J. Caban, A. F. Suffredini, T. N. Palmore, and D. J. Mollura, "Learning shape and texture characteristics of CT tree–in–bud opacities for CAD systems," in *Medical Image Computing and Computer-Assisted Intervention — MICCAI 2011*, Lecture Notes in Computer Science Vol. 6893, edited by G. Fichtinger, A. Martel, and T. Peters (Springer, Berlin, Heidelberg, 2011), pp. 215–222.
[27]A. Depeursinge, A. Foncubierta-Rodríguez, D. Van De Ville, and H. Müller, "Multiscale lung texture signature learning using the Riesz transform," in *Medical Image Computing and Computer–Assisted Intervention MICCAI 2012*, Lecture Notes in Computer Science Vol. 7512 (Springer, Berlin, Heidelberg, 2012), pp. 517–524.
[28]M. Unser, N. Chenouard, and D. Van De Ville, "Steerable pyramids and tight wavelet frames in $L_2(\mathbb{R}^d)$," IEEE Trans. Image Process. **20**, 2705–2721 (2011).
[29]J. H. Friedman, T. Hastie, and R. Tibshirani, "Regularization paths for generalized linear models via coordinate descent," J. Stat. Software **33**, 1–22 (2010).
[30]C.-C. Chang and C.-J. Lin, "LIBSVM: A library for support vector machines," ACM Trans. Intell. Syst. Technol. **2**, 1–27 (2011).
[31]N. Simon, J. H. Friedman, T. Hastie, and R. Tibshirani, "Regularization paths for Cox's proportional hazards model via coordinate descent," J. Stat. Software **39**, 1–13 (2011).
[32]L. Evers and C.-M. Messow, "Sparse kernel methods for high–dimensional survival data," Bioinformatics **24**, 1632–1638 (2008).
[33]A. Depeursinge, A. Foncubierta-Rodríguez, D. Van De Ville, and H. Müller, "Rotation–covariant texture learning using steerable Riesz wavelets," IEEE Trans. Image Process. **23**, 898–908 (2014).
[34]J. Portilla and E. P. Simoncelli, "A parametric texture model based on joint statistics of complex wavelet coefficients," Int. J. Comput. Vision **40**, 49–70 (2000).
[35]F. E. Harrell, K. L. Lee, and D. B. Mark, "Tutorial in biostatistics multivariable prognostic models: Issues in developing models, evaluating assumptions and adequacy, and measuring and reducing errors," Stat. Med. **15**, 361–387 (1996).
[36]J. Xu, S. Napel, H. Greenspan, C. F. Beaulieu, N. Agrawal, and D. Rubin, "Quantifying the margin sharpness of lesions on radiological images for content–based image retrieval," Med. Phys. **39**, 5405–5418 (2012).
[37]R. Achanta, A. Shaji, K. Smith, A. Lucchi, P. Fua, and S. Süsstrunk, "SLIC superpixels compared to state–of–the–art superpixel methods," IEEE Trans. Pattern Anal. Mach. Intell. **34**, 2274–2282 (2012).
[38]Y. Tao, L. Lu, M. Dewan, A. Y. Chen, J. Corso, J. Xuan, M. Salganicoff, and A. Krishnan, "Multi–level ground glass nodule detection and segmentation in CT lung images," in *Medical Image Computing and Computer-Assisted Intervention — MICCAI 2009*, Lecture Notes in Computer Science Vol. 5762, edited by G.-Z. Yang, D. Hawkes, D. Rueckert, A. Noble, and C. Taylor (Springer, Berlin, Heidelberg, 2009), pp. 715–723.